Available online at www.sciencedirect.com
ScienceDirect
International Journal of Heat and Mass Transfer 50 (2007) 3599–3615
International Journal of HEAT and MASS TRANSFER
www.elsevier.com/locate/ijhmt

Natural convection for large temperature gradients around a square solid body within a rectangular cavity

M. Bouafia, O. Daube *

LMEE – Université d'Evry, CE 1455 Courcouronnes, 91020 Evry cedex, France

Received 6 October 2005; received in revised form 2 May 2006

Abstract

A numerical study of natural convection in cavity filled with air has been carried out under large temperature gradient. The flows under study are generated by a heated solid body located close to the bottom wall in a rectangular cavity with cold vertical walls and insulated horizontal walls. They have been investigated by direct simulations using a two-dimensional finite volume numerical code solving the time-dependent Navier–Stokes equations under the low Mach number approximation. This model permits to take into account large temperature variations unlike the classical Boussinesq model which is valid only for small temperature differences. We were particularly interested in the first transitions which occur when the Rayleigh number is increased for flows in cavities of aspect ratio $A = 1, 2, 4$. Starting from a steady state, the results obtained for $A = 1$ and $A = 4$ show that the first transition occurs through a supercritical Hopf bifurcation. The induced disturbances determined for weakly supercritical regimes indicate the existence of two instability types driven by different physical mechanisms: shear and buoyancy-driven instabilities, according to whether the flow develops in a square or in a tall cavity. For $A = 2$, the flow undergoes a pitchfork bifurcation leading to an asymmetric steady state which in turn becomes periodic via a supercritical Hopf bifurcation point. In both cases, the flow is found to be strongly deflected towards one vertical wall and instabilities are found to be of shear layers type.

1. Introduction

The study of buoyant plumes induced by temperature differences between a fluid and its surroundings is of importance not only to scientific understanding but also to engineering practice. Mechanisms of buoyancy-induced convection become more complex when there are interactions of the flow with solid boundaries. This paper deals with the analysis of a transitional plane plume originating from a square obstacle immersed inside a rectangular cavity. Three aspect ratios have been considered in this study. It should be noticed that all the configurations present a reflection symmetry and that the bifurcations which occur when the Rayleigh number increases will be analyzed through this symmetry breaking.

Laminar and turbulent plane plumes arising from horizontal line sources in infinite or semi-infinite medium have drawn the attention of many investigations in the past: from classical self-similar solutions [1–3] to linear stability analysis [4–7] for earlier theoretical studies, added to several experimental investigations carried out during the same period and relating to plume oscillations [4,6,8–11].

Many observations of laminar plume flows have indicated a regular swaying motion in a plane perpendicular to the axis of the source [10,11]. Following these observations, the stability problem of a freely rising plume was first studied by Pera and Gebhart [4] using the linear stability theory based on quasi-parallel flows. This theory predicts the amplification characteristics of small periodic disturbances as a function of frequency β and Grashof number Gr_x. The authors obtained a neutral stability curve for $Pr = 0.7$ but failed to find a critical Grashof number. They also made experimental observations using a Mach–Zender

* Corresponding author.
E-mail address: olivier.daube@iup.univ-evry.fr (O. Daube).

0017-9310/$ - see front matter © 2006 Elsevier Ltd. All rights reserved.
doi:10.1016/j.ijheatmasstransfer.2006.05.013

Nomenclature

Greek symbols

$\epsilon = \Delta T/2T_0$ normalized temperature difference
κ thermal conductivity
μ dynamic viscosity
π reduced pressure
ρ density
c_p, c_v specific heat capacities
$\alpha = \frac{\kappa}{\rho c_p}$ thermal diffusivity

Subscripts and superscripts

0 values at temperature difference
* Adams–Bashforth extrapolation
h hot
c cold
$A = H/L$ aspect ratio
H height
L width
L_0 reference length
$\overline{P}$ mean thermodynamic pressure
$P_0 = \rho_0 V_0^2$ reference pressure
$Pr = \frac{\mu_0}{\rho_0 \alpha_0}$ Prandtl number
$Ra = 2\rho_0 \varepsilon g L_0^3/\mu_0 \alpha_0$ Rayleigh number
$t_0 = L_0/V_0$ reference time
T non-dimensional temperature
$T_0 = (T_h + T_c)/2$ reference temperature
$V_0 = \frac{\mu_0}{\rho_0 L_0}\sqrt{Ra}$ reference velocity
u horizontal component of the non-dimensional velocity
v vertical component of the non-dimensional velocity

interferometer to observe the disturbances as they were convected downstream. The experimental results show that sufficiently high frequency disturbances are stable as they are convected downstream. Later, calculations of the same problem have been carried out by Haaland and Sparrow [5] taking into account non-parallel and higher-order effects of the base flow in the linear stability analysis. The authors obtained a lower branch of neutral curve and then a critical Grashof number. Their results show that the unstable region is smaller than that obtained from the quasi-parallel theory. The stability problem of non-parallel flows were also investigated by Wakitani [7] using the method of multiple scales. This method considers that the various disturbance quantities have different amplification rates. Their results relating to the amplification rate of disturbances within unstable regions show a substantial deviation from that predicted by the quasi-parallel theory.

The determination of the critical Grashof number corresponding to the transition from laminar to turbulent in a freely rising plume has been investigated experimentally by Bill and co-workers [8,10] among others. The authors defined a local Grashof number based on the vertical distance along the plume and the heat rate input. The onset of transition considered as the initial appearance of the turbulent bursts, occurred at a Grashof number of $Gr_x = 5 \times 10^8$ according to [10] and at $Gr_x = 11.2 \times 10^8$ for [8]. The later attributed the discrepancy to the weak precision of the interferometer for small local disturbances. Moreover, several studies have examined the interaction between buoyant plumes and neighbouring vertical surfaces and have observed a deflection of plume towards the surface [12,13]. This Coanda effect is seen to be a consequence of constrained entrainment of the fluid feeding the plume due to the presence of the vertical surface.

Although there are many studies in infinite or semi-infinite medium, few information is available about thermal plumes in confined geometry where influence of boundaries and initial conditions must be taken into account. The behaviour of plumes in confined geometry can be simulated numerically using direct numerical simulations (DNS) which allows for parametric studies on such flows for engineering purposes. The few numerical studies found in the literature consider flows under the Boussinesq approximation. Among them, one can notice works carried out by Desrayaud and Lauriat [14] where considerable research efforts have been devoted to unsteady thermal plumes in many geometric configurations. The authors considered two-dimensional flows generated by a horizontal line source inside a rectangular cavity with adiabatic sidewalls and cold top and bottom walls. By varying the depth of immersion, the aspect ratio and the Rayleigh number, the authors have shown the existence of three different physical mechanisms leading to chaotic flows by a succession of bifurcation points. All the configurations considered show a base flow which consists of two symmetric counter-rotating rolls around an ascending thermal plume arising above the line source.

A first scenario is found for aspect ratio equal to 1 and depths of immersion smaller than the width. The underlying mechanism of the onset of instabilities is the destabilization of a significant mass of fluid below the line source. The periodic flow appears through a supercritical Hopf bifurcation characterized by a frequency proportional to the height of the fluid under the source. A second scenario is found only if the aspect ratio $A \leqslant 1$ and if the layer of fluid below the source is small enough and the plume reaches the top wall. In this case, the plume is bounded below by a stable conducting layer of fluid. The flow undergoes a supercritical Hopf bifurcation leading to a periodic motion with a high fundamental frequency. This motion is followed by a quasi-periodic regime before a weakly turbulent regime arises via an intermittent route to chaos. A

third scenario is found in cavities of aspect ratio $A = 2$ and for depths of immersion of the source greater than the width. The symmetric flow undergoes a pitchfork bifurcation leading to a deflection of the plume towards one vertical wall. The symmetry breaking is driven by the destabilization of an upper unstable layer of motionless fluid above the plume. An increase of the Rayleigh number leads to a periodic motion with a very low frequency via a subcritical Hopf bifurcation.

Two-dimensional convection flows have also been investigated numerically by Zia et al. [15] in a differentially heated cavity containing a heat source above the bottom surface of the cavity, and by Horvat et al. [16] for a low-viscosity flow with zero thermal diffusivity. In this paper, our approach is close to the one used by Desrayaud and Lauriat [14]. The difference lies in taking into account large temperature differences between the source and the vertical walls of the cavity. Because of the large density variation involved, the usual Boussinesq approximations are no longer valid and the compressible Naviers–Stokes equations have to be considered. However, since these equations contain acoustic waves, the numerical stability criterion is too much restrictive because of the wide disparity between the time scales associated with convection and the propagation of acoustic waves. A solution to this problem consists of the filtering of these waves using the low Mach approximation of the Navier–Stokes equations [18]. This model decouples pressure fluctuations from density fluctuations making the resulting equations similar to the incompressible case. In particular, acoustic waves are excluded whereas gravity waves may still occur.

The Low-Mach Number equations (LMN) have been used in many studies to investigate the effects of large temperature variations in natural convection flows [19–21] and also for near-critical fluids [22,23]. In the present study, the LMN equations supplemented by the state equation for ideal gases are used to investigate the flows in 2D-cavities of aspect ratio $A = 1, 2, 4$. The plumes arise from a hot square solid immersed in the vertical centerline of the cavity which have isothermal vertical walls and insulated horizontal walls. This paper is organized as follows. The next section recalls the governing equations and the numerical method. Section 3 is devoted to results obtained in steady and oscillatory regimes for each configuration. The paper ends with a summary of major conclusions.

2. Problem formulation

2.1. Governing equations

Consider a two-dimensional cavity of width L and height H filled with a viscous fluid. The gravity is directed downwards the y-axis. A solid body of square section is immersed on the vertical centerline of the cavity close to the bottom wall. Its dimensions in horizontal and vertical directions are $l_x = l_y = L/8$. The body is considered as a heating source with a uniform temperature T_h. The vertical walls of the cavity are maintained at the cold temperature T_c ($T_c < T_h$), while the top and the bottom walls are thermally insulated. The working fluid is air which is initially at a uniform temperature $T_0 = (T_h + T_c)/2$ and pressure P_0. It is assumed to be an ideal gas with constant specific heats c_p and c_v of ratio $\gamma = 1.4$. Its dynamic viscosity μ and thermal conductivity κ are allowed to depend on temperature.

Since we are primarily interested in flows induced by large temperature differences, we have adopted the low Mach number model described by Chenoweth and Paolucci [19] and used later by Le Quéré [20]. In this model, the complete Naviers–Stokes equations are expanded in powers of the small parameter M^2 (M is the Mach number). Paolucci [18] showed that the pressure may be divided into two parts: a mean thermodynamic pressure which depends only on time and a dynamic pressure not coupled with the density fluctuations preventing the propagation of the acoustic waves. The equations are made dimensionless by scaling length, time, temperature, pressure and velocity by reference quantities: $L_0 = L$, $t_0 = L_0/V_0$, $T_0 = (T_h + T_c)/2$, $P_0 = \rho_0 V_0^2$, $V_0 = \frac{\mu_0}{\rho_0 L_0}\sqrt{Ra}$. The thermophysical properties (density, dynamic viscosity, thermal conductivity, thermal diffusivity) are scaled by ρ_0, μ_0, κ_0, α_0 where the subscript 0 denotes values at the reference temperature T_0. Finally, according to Le Quéré et al. [20], the governing equations in the dimensionless form are

$$\frac{\partial \rho}{\partial t} + \nabla \cdot (\rho \boldsymbol{V}) = 0 \tag{1}$$

$$\rho\left(\frac{\partial \boldsymbol{V}}{\partial t} + (\boldsymbol{V}\cdot\nabla)\boldsymbol{V}\right) = -\nabla \Pi + (Ra)^{-1/2}\nabla\cdot\bar{\bar{\tau}} - Pr^{-1}\frac{\rho-1}{2\varepsilon}\boldsymbol{y} \tag{2}$$

$$\rho\left(\frac{\partial T}{\partial t} + (\boldsymbol{V}\cdot\nabla)T\right) = \frac{1}{Pr\,Ra^{1/2}}\nabla\cdot(\kappa\nabla T) + \frac{\gamma-1}{\gamma}\frac{\mathrm{d}\overline{P}}{\mathrm{d}t} \tag{3}$$

$$\overline{P} = \rho T \tag{4}$$

Note that we have five equations for six unknowns ρ, u, v, T, Π and $\overline{P}$. The necessary additional equation is given by calculating the term $\mathrm{d}\overline{P}/\mathrm{d}t$. Mass conservation equation (1), combined with energy equation (3) and state equation (4) permit to write the divergence of velocity in the form given by Eq. (5). When integrated over the fluid domain, this equation leads to Eq. (6) for $\mathrm{d}\overline{P}/\mathrm{d}t$

$$\nabla\cdot\boldsymbol{V} = \frac{\nabla\cdot(\kappa\nabla T)}{Pr\,Ra^{1/2}\overline{P}} - \frac{1}{\gamma\overline{P}}\frac{\mathrm{d}\overline{P}}{\mathrm{d}t} \tag{5}$$

$$\frac{\mathrm{d}\overline{P}}{\mathrm{d}t} = \frac{\gamma}{A\,Pr\,Ra^{1/2}}\int_\Gamma \kappa\frac{\partial T}{\partial n}\,\mathrm{d}S \tag{6}$$

$\boldsymbol{V}$ is the velocity vector of components (u, v), $\bar{\bar{\tau}} = \mu(\nabla\boldsymbol{V} + (\nabla\boldsymbol{V})^t - \frac{2}{3}(\nabla\boldsymbol{V})I$ the viscous stress tensor, $\Pi = (P - \overline{P} + \rho_0 g y)/\rho_0 V_0^2$ the reduced pressure, $\overline{P}(t)$ the mean thermodynamic pressure, $\varepsilon = \Delta T/2T_0$ the normalized temperature difference where ΔT is the temperature difference $(T_h - T_c)$ between the obstacle and the sidewalls and $A = H/L_0$ the aspect ratio. The independent dimensionless

parameters are the Prandtl number and the Rayleigh number defined at the reference temperature T_0

$$Pr = \frac{\mu_0}{\rho_0 \alpha_0}; \quad Ra = 2\rho_0 \varepsilon g L_0^3 / \mu_0 \alpha_0 \tag{7}$$

where $\alpha_0 = \kappa_0/\rho_0 c_p$ is the thermal diffusivity. The system of equations is closed by Sutherland's law for the dynamic viscosity μ

$$\mu(T) = T^{3/2}\frac{1+S_\mu}{T+S_\mu} \tag{8}$$

and since the Prandtl number is assumed constant in this study, the thermal conductivity κ is given by

$$\kappa(T) = \mu(T) \tag{9}$$

where $S_\mu = 0.368$ for $\varepsilon < 0.6$ and $T_0 \in [210\ \text{K}, 673\ \text{K}]$. The computational domain is defined for a rectangular cavity $\Omega = [0,1]\times[0,A]$. At the boundaries, the no-slip conditions for velocities are coupled to temperature conditions

$$\begin{cases} T = 1-\varepsilon & \text{at } x = 0 \\ T = 1-\varepsilon & \text{at } x = 1 \\ T = 1+\varepsilon & \text{on the obstacle} \\ \frac{\partial T}{\partial n} = 0 & \text{at } y = 0 \text{ and } y = H/L \end{cases} \tag{10}$$

2.2. Numerical modelling

The governing equations are solved numerically by a finite-volume scheme using the usual staggered arrangement on a non-uniform grid. The resulting mesh leads to a grid layout strongly refined close to the source and the walls of the cavity. The time derivative is approximated using a second order backward Euler scheme in which the diffusive and viscous linear terms are implicitly treated while the convective nonlinear terms are explicitly treated using an Adams–Bashforth extrapolation. For instance, the fully time discretized formulations for the energy equation read

$$\rho^n\left(\frac{3T^{n+1}-4T^n+T^{n-1}}{2\Delta t} + (\boldsymbol{V}.\nabla T)^*\right) = Ra^{-1/2}\nabla(\kappa^*\nabla T^{n+1}) + \left(\frac{\gamma-1}{\gamma}\right)\frac{\mathrm{d}\overline{P}^*}{\mathrm{d}t}$$

where * refers to Adams–Bashforth extrapolation ($f^* = 2f^n - f^{n-1}$).

A similar approach is then applied to the momentum equations. This process results in Helmholtz-type equations for T^{n+1}, u^{n+1} and v^{n+1}

$$(\sigma_T\overline{\overline{\mathbf{I}}} - \nabla\cdot\kappa^*\nabla)T^{n+1} = S_T^{n,n-1} \tag{11}$$

$$(\sigma_V\overline{\overline{\mathbf{I}}} - \nabla\cdot\mu^{n+1}\nabla)u^{n+1} = -\sqrt{Ra}\,\nabla\Pi^{n+1} + S_u^{n,n-1} \tag{12}$$

$$(\sigma_V\overline{\overline{\mathbf{I}}} - \nabla.\mu^{n+1}\nabla)v^{n+1} = -\sqrt{Ra}\,\nabla\Pi^{n+1} + S_v^{n,n-1} \tag{13}$$

$$\nabla\cdot V = S_D^{n,n-1} \tag{14}$$

where $\overline{\overline{\mathbf{I}}}$ is the identity tensor, $\sigma_T = 3\rho^n Pr\sqrt{Ra}/2\Delta t$ and $\sigma_V = 3\rho^{n+1}\sqrt{Ra}/2\Delta t$. $S_T^{n,n-1}$, $S_u^{n,n-1}$, $S_v^{n,n-1}$ and $S_D^{n,n-1}$ are source terms depending on time steps n and $n-1$.

2.3. Time marching procedure

Assuming the flow is known at time levels $(0,\ldots,n)$, the different stages to compute the flow at $(n+1)$ are respectively:

- Determination of the temperature field from (3) using extrapolated values of κ^* and $(\mathrm{d}\overline{P}/\mathrm{d}t)^*$.
- Calculation of the new physical properties κ^{n+1} and μ^{n+1}.
- Calculation of $\overline{P}^{n+1}$ using mass conservation (see [20]) and of $(\mathrm{d}\overline{P}/\mathrm{d}t)^{n+1}$ using Eq. (6). The divergence of velocity S_D^{n+1} in Eq. (13) can then be computed at time level $(n+1)$.
- Calculation of ρ^{n+1} by using Eq. (4).
- Resolution of the momentum equations by using a "projection" method derived from the classical projection methods for incompressible flows [24].
- *Prediction*. Computation of a provisional velocity field satisfying the following equation over the computational domain Ω of boundary Γ:

$$(\sigma_V\overline{\overline{\mathbf{I}}} - \nabla\cdot\mu^{n+1}\nabla)\boldsymbol{V}^* = -Ra^{1/2}\nabla\Pi^n + \boldsymbol{S}^{n,n-1} \tag{15}$$

- *Projection*. Computation of an auxiliary function ϕ satisfying

$$\begin{cases} \rho^{n+1}(\boldsymbol{V}^{n+1} - \boldsymbol{V}^*) = \nabla\Phi & \text{in } \Omega \\ \nabla\cdot\boldsymbol{V}^{n+1} = D^{n,n-1} & \text{in } \Omega \\ \boldsymbol{V}^{n+1}\cdot\boldsymbol{n} = 0 & \text{on } \Gamma \end{cases} \tag{16}$$

This leads to the resolution of the diffusive problem

$$\begin{cases} \nabla\cdot\left(\frac{1}{\rho^{n+1}}\nabla\Phi\right) = S_D^{n,n-1} - \nabla\cdot\boldsymbol{V}^* & \text{in } \Omega \\ \frac{\partial\Phi}{\partial n} = 0 & \text{on } \Gamma \end{cases} \tag{17}$$

The resolution of the Poisson equation (16) is done through a multigrid acceleration procedure. The velocity $\boldsymbol{V}$ and the pressure Π are then calculated from the expressions

$$\boldsymbol{V}^{n+1} = \boldsymbol{V}^n + \frac{1}{\rho^{n+1}}\nabla\Phi \tag{18}$$

$$\Pi^{n+1} = \Pi^n - \frac{3\Phi}{2\Delta T} \tag{19}$$

2.4. Validation of the code

The code has been tested in some relevant benchmark cases corresponding to the non-Boussinesq convection in a differentially heated square cavity [29]. Tests have been carried out for a normalized temperature difference $\varepsilon = 0.6$ and for $Ra = 10^6$ and 10^7. For these values of the parameters, the flow tends to a steady state. Two cases

have been studied, the first for constant fluid properties, the second using the Sutherland's law for viscosity and a constant Prandtl number. Results obtained by our code reveal a very good agreement with the reference solutions resulting from this benchmark.

The present study is devoted to investigate unsteady flows generated by a square source located in the mid-plane of cavities with aspect ratios $A = 1, 2, 4$. The influence of the grid size has been analyzed by testing several non-uniform meshes. For all geometries, the grid layout was refined close to the walls and around the heat source by using Chebychev collocation points in both horizontal and vertical directions. After a number of trial numerical experiments, a (296×296) grid for the square cavity was considered as a good compromise between stability or accuracy requirements on one hand and computational costs on the other hand.

The influence of the time step has also been considered. Different values were tested by comparing the solutions in terms of amplitude and frequency in periodic regimes. When considering both these aspects as well as the relatively long computer simulations times involved, it was finally decided to use a time step $\Delta t = 0.004$ for values of Ra close to the first bifurcation point ($Ra < 7 \times 10^6$ in square cavity). We have verified that decreasing the time step to $\Delta t = 0.002$ gave a decrease of amplitude of 4% and an increase of frequency of 1.5% for $Ra = 6.8 \times 10^6$. When decreasing more the time step from $\Delta t = 0.002$–5×10^{-4}, the results in terms of frequency and amplitude remain constant.

For the rectangular cavity of aspect ratio $A = (H/L) = 4$, a similar study leads us to take a (296×440) non-uniform grid. Using this mesh, the flow was found to be periodic at Ra between 1.2×10^4 and 1.3×10^4. In view of the moderate values of the Rayleigh number at which instabilities occurs, time steps used are $\Delta t = 0.01$ for $Ra < 1.4 \times 10^4$. For the cavity with aspect ratio $A = 2$, the computations have been performed with a (296×296) non-uniform grid and time steps varying from 0.007 to 0.004 for values of Ra within the range $[4 \times 10^4, 1.5 \times 10^6]$.

2.5. Methodology

The numerical experiments were carried out as follows. For each considered value of the aspect ratio, the cavity is filled with a fluid at uniform reference temperature $T_0 = (T_h + T_c)/2$. At instant $t = 0$, the body and the lateral walls are set to their final temperatures T_h and T_c and a first computation is performed for a sufficiently low value of the Rayleigh number in order to reach a steady flow. This steady state is in turn used as an initial condition for a subsequent computation at a larger value of Ra and the procedure is resumed for increasing values of the Rayleigh number. When the flow becomes unsteady, its temporal characteristics are analyzed from time series of temperature and velocity values at selected sampling points.

It must be noticed that all the studied configurations present a reflection symmetry with respect to the vertical centerline of the cavity. The bifurcations which occur when the Rayleigh number increases will thus be analyzed through this symmetry breaking. When it was found necessary, a symmetric base flow (possibly unstable) has been computed by considering the half of the domain and imposing symmetric boundary conditions on the central vertical axis.

3. Results and discussion

The parameters governing the plume formation are the Rayleigh number, the aspect ratio A, the location of the heating source, the normalized temperature difference ε and the initial conditions. A quite extensive analysis would be needed to cover all the possible effects of each parameter. In this study, the following values were maintained constant for all the configurations. The source center is located at position $M_s(0.5, 0.25)$ and the normalized temperature difference is $\varepsilon = 0.2$. This value corresponds to an actual temperature difference $\Delta T = 120$ K between the source and the vertical walls and to a reference temperature $T_0 = (T_h + T_c)/2 = 300$ K. This temperature difference is much larger than the commonly admitted limits of validity for the Boussinesq approximation which is about 30 K for air in the standard atmospheric conditions. To validate this point, Boussinesq computations reported in Section 3.2.2 show that the nature of the first bifurcation is strongly affected by non-Boussinesq effects. However, we did not make an extensive study of larger values of ϵ though the benchmark for the differentially heated cavity was computed for $\epsilon = 0.6$.

In all the considered configurations, the expected base flow consists first of a hot fluid rising above the heating source in the form of an ascending thermal plume. In order to satisfy the zero mass flux condition, the flow then returns to the source forming two counter-rotating recirculations movements. In addition, secondary flows may occur depending on the aspect ratio as will be shown later.

3.1. Cavity $A = 1$

3.1.1. Symmetric steady flow

Flow structure: For sufficiently low values of Ra, the flow reaches an asymptotic steady state exhibiting a symmetric motion about the vertical centerline of the cavity. Typical velocity fields and isotherms are displayed in Fig. 1 for $Ra = 5 \times 10^6$. The flow pattern is characterized by a primary flow which consists of two counter-rotating recirculations flows delimited by a vertical thermal plume. In this primary flow (zone A in Fig. 1(a) and (b)), the hot fluid rises above the source until it reaches the top wall, then moves outwards along the horizontal wall before moving downwards along the sidewalls inducing boundary layers in which it is cooled. When it arrives at the bottom wall, the fluid returns to the source, almost horizontally to it. The core of the primary flow is stratified in its lower part (zone B in Fig. 1(a) and (b)) and contains two small

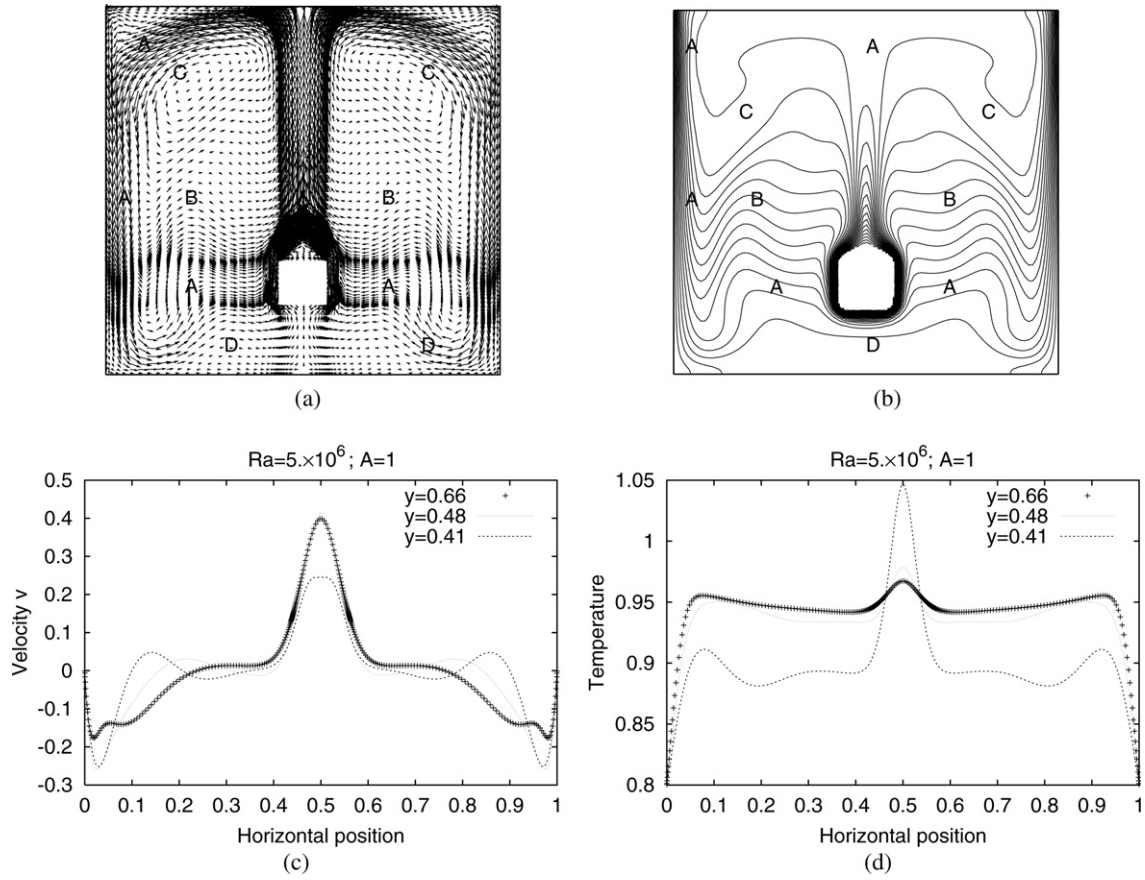

Fig. 1. (a, b) Velocity field and isotherms at steady state in the square cavity for $Ra = 5.0 \times 10^6$, (c, d) the corresponding horizontal profiles of vertical velocity and temperature.

eddies, one on each side of the plume, in its upper part (zone C in Fig. 1(a) and (b)). The primary flow delimits a fluid layer below the source which is almost at rest and uniform in temperature. Moreover, the primary flow is distinguished by marked sheared zones located in the plume and the boundary layers. These shear layers characterized by large velocity gradients are clearly visible in the horizontal profiles of temperature and vertical velocity plotted for various heights above the source (see Fig. 1(c) and (d)).

3.1.2. Unsteady periodic flow

The flow becomes periodic beyond a critical value of the Rayleigh number located in the range $[5.5 \times 10^6, 6 \times 10^6]$. For instance, Fig. 2(a) shows the time evolutions of the horizontal component u of the velocity for $Ra = 6.8 \times 10^6$ at two points on the vertical centerline. These signals are clearly periodic and a Fourier analysis yields a fundamental frequency $f_1 = 0.197$ with its two first odd harmonics (Fig. 2(b)). This behaviour is related to the

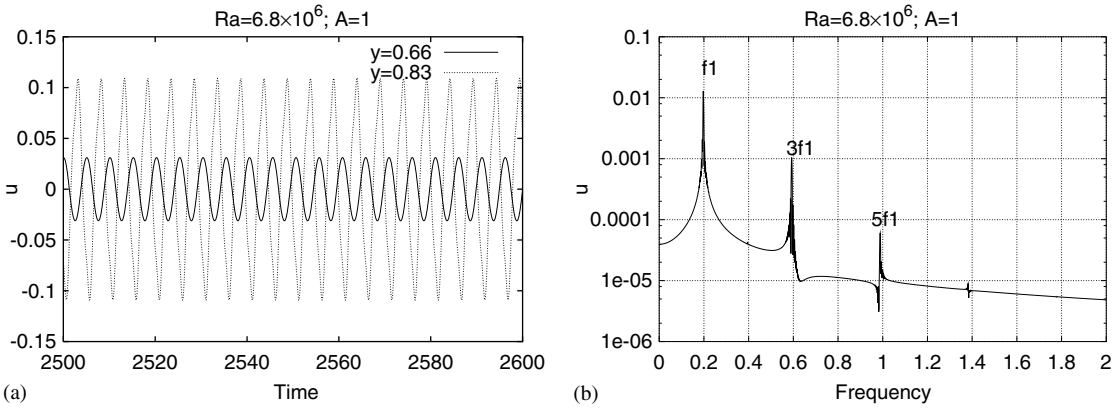

Fig. 2. (a) Time evolutions of the horizontal velocity at points $M_1(0.5, 0.66)$ and $M_2(0.5, 0.83)$ and (b) power spectrum of the u-velocity at point $M_2(0.5, 0.83)$.

breaking of the reflection symmetry associated with the bifurcation.

Moreover, computations not reported here have shown that the closer the Rayleigh number is to its critical value, the longer is the time for attaining the asymptotic flow. This suggests that the onset of unsteady solutions is due to a supercritical Hopf bifurcation. This is confirmed by the fact that no hysteresis effect could be found when the Rayleigh number was decreased from $Ra = 6 \times 10^6$ to $Ra = 5 \times 10^6$.

Flow structure: This transition is characterized by a breaking of the reflection symmetry which induces a swaying motion of the thermal plume. To illustrate this behaviour, results for $Ra = 6.8 \times 10^6$ are presented. Typical instantaneous velocity fields are shown in Fig. 3(b)–(f) evenly distributed over one time period. From these plots, it can be seen that the upper part of the rising plume oscillates horizontally once to the right once to the left side of the cavity. During one period, the secondary upper rolls inside the primary flow (see Section 3.1.1), break into two smaller counter-rotating rolls and afterwards merge again (see Fig. 3(b), (d) and (f)). The fluid layer below the source remains almost at rest although the convective motion extends slightly to the bottom of the cavity. Time averaged velocity field showing a symmetric pattern about the vertical centerline, is plotted in Fig. 3(a) by integrating instantaneous fields over a sufficiently long time (400 non-dimensional time units).

Base flow and flow fluctuations: In order to examine the instability mechanisms, we have first calculated the symmetric unstable base flow by imposing symmetry boundary conditions on the vertical centerline and then computed the temporal fluctuations with respect to this base flow by subtracting the symmetric base solutions from instantaneous fields. Before considering the fluctuations, it may be noticed that the symmetric unstable base flow is slightly different from the symmetric time averaged flow.

The spatial distributions of the fluctuations are displayed in Fig. 4 for $Ra = 6.8 \times 10^6$ at eight instants over one oscillation period. The temperature field corresponding to the base solution is also presented in Fig. 4(e). These plots indicate that the maximum of disturbances are confined within the plume and to a lesser extent in the boundary layers and the core of the primary flow. The disturbances consist of structures of alternate sign distributed simultaneously in the two halves of the cavity whereas the layer of fluid below the source remains still stable.

The instabilities which occur in zones with large gradient velocity with an inflection point may be identified with shear instabilities and move along the primary flow direction. They first arise just above the source in the form of detached blobs, then are convected in the plume until the upper surface is reached. At the top wall, they spread out horizontally to the left and to the right, then sink along the sidewalls before vanishing when approaching the bottom wall. The results for $Ra = 6.8 \times 10^6$ indicate a range of temperature fluctuations between $[-0.03, +0.03]$ with maximum values located within the plume.

3.2. Cavity $A = 2$

3.2.1. Symmetric steady flow

As usual, a symmetric steady flow is found for low values of the Rayleigh number Ra, in this case for $Ra < 4.5 \times 10^4$. The main characteristics of the flow for $Ra = 4.0 \times 10^4$ are deduced from Fig. 5(a)–(c) in which

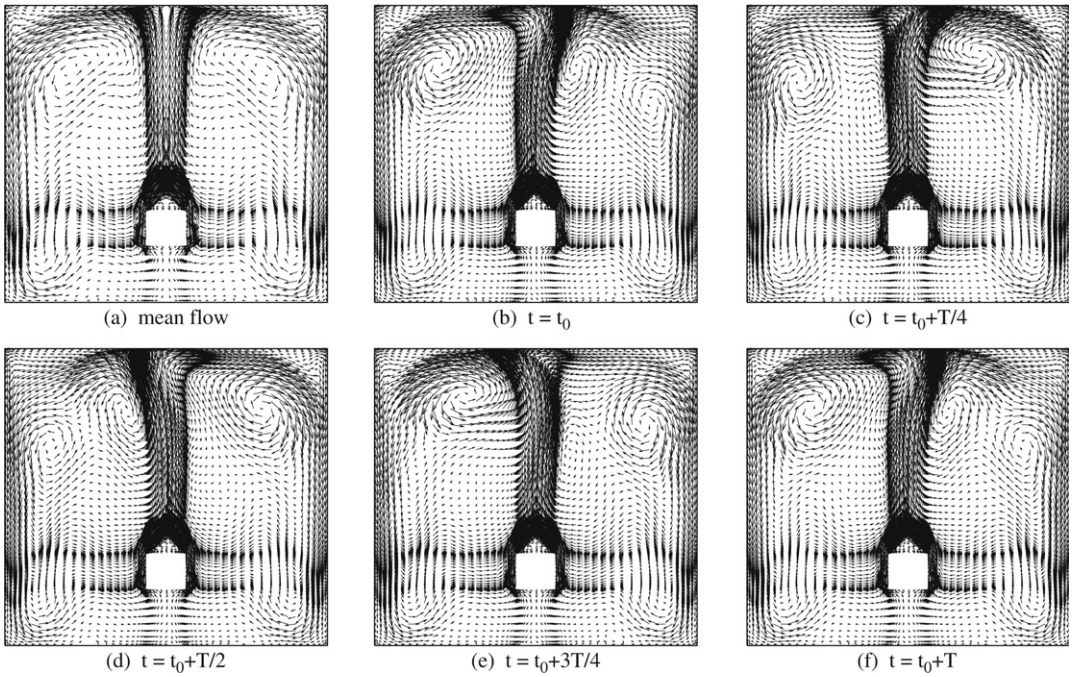

Fig. 3. (a) Mean velocity field, (b–f) instantaneous fields at five instants over one time period for $Ra = 6.8 \times 10^6$.

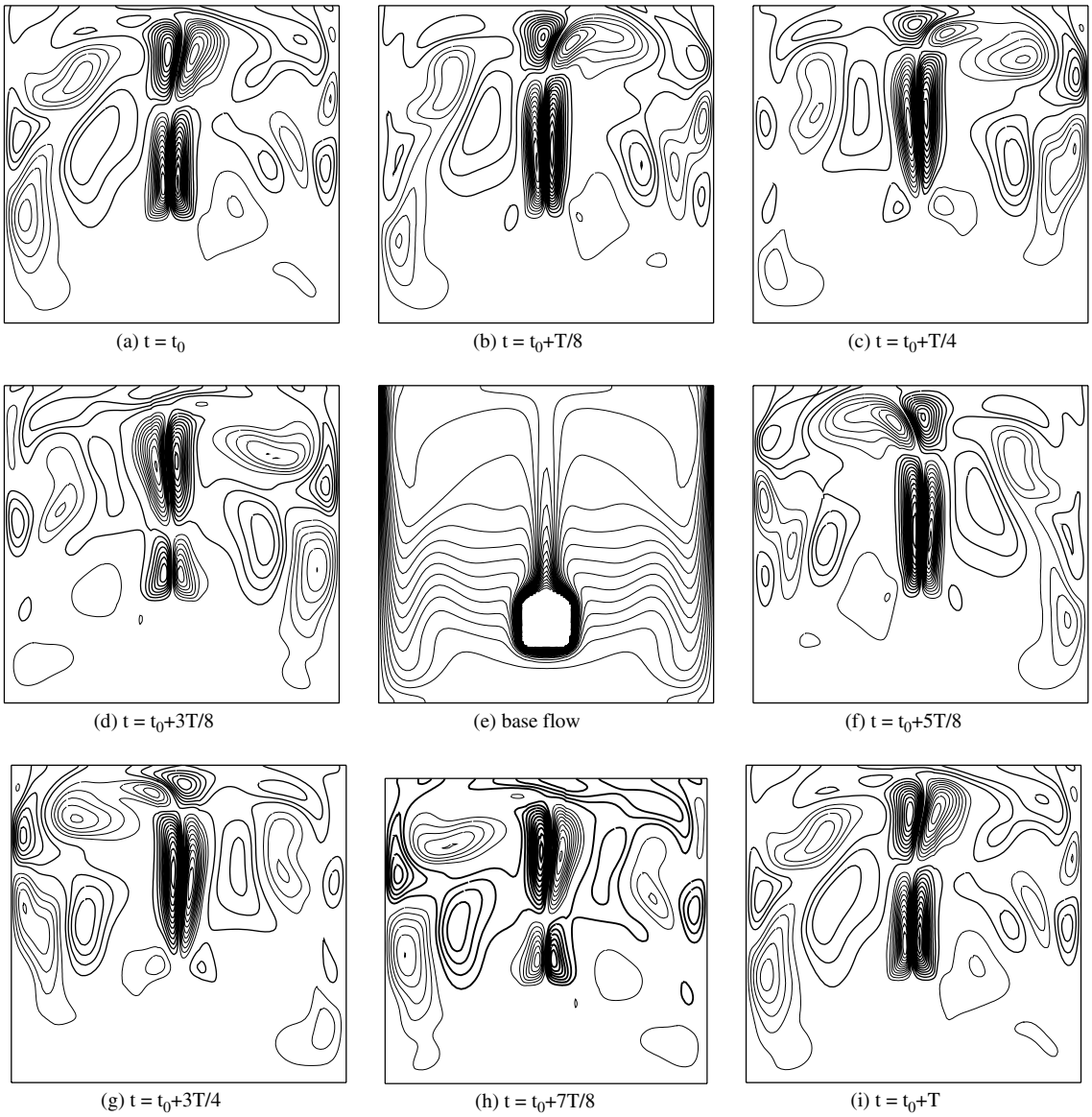

Fig. 4. (a–d) and (f–i) Contours of temperature fluctuations at eight instants over one time period, (e) base flow temperature; thin (thick) lines for positive (negative) values; variation range $[-0.03, +0.03]$ for $Ra = 6.8 \times 10^6$.

typical velocity, streamlines and temperature fields are displayed, and from Fig. 5(d) and (e) in which horizontal profiles of temperature and vertical velocity V_y are plotted.

- The flow consists essentially of two symmetric recirculation zones delimited by an ascending thermal plume which extends up to the upper wall of the cavity (Fig. 5(b)). There exists a small layer of quiet fluid just below the heating source in which heat transfer is essentially conductive.
- Unlike the square cavity case, no stratification may be observed in the flow (Fig. 5(c)).
- The temperature and v profiles are typical of shear layers developing along the sidewalls, at least in the upper part ($y > 1$). These layers are rather thick because of the low value of the considered Rayleigh number (see Fig. 5(d) and (e)).

3.2.2. Asymmetric steady flow

When the Rayleigh number is increased beyond a critical value Ra_c, the steady symmetric flow looses its stability, yielding an asymmetric steady solution. This transition appears to be a pitchfork bifurcation whose threshold lies at a critical value within the range $[4.5 \times 10^4, 5 \times 10^4]$.

Flow structure: The structure of the bifurcated flow is illustrated in Fig. 6(a)–(c) by velocity, temperature fields and streamlines for $Ra = 1.1 \times 10^5$. Two large recirculation zones may still be observed, but they are no longer symmetric with respect to the central axis. The main point is the onset of the well known Coanda effect which induces a deflection of the thermal plume towards one or the other sidewall, depending on the initial conditions. To check this point, the symmetric steady flow – within roundoff and convergence errors – for $Ra = 5 \times 10^4$ was flipped with respect to the vertical centerline, yielding another initial

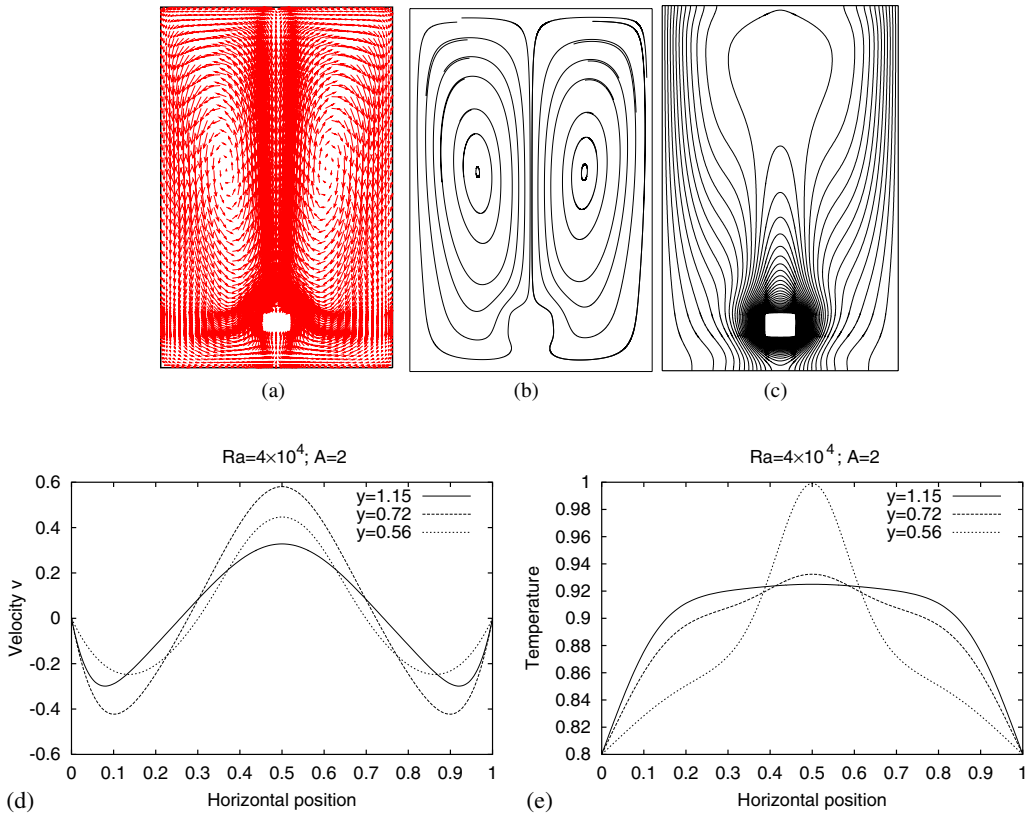

Fig. 5. (a–c) Velocity field, streamlines and isotherms at steady state in cavity $A = 2$ for $Ra = 4. \times 10^4$, (d) and (e) the corresponding temperature and vertical velocity profiles.

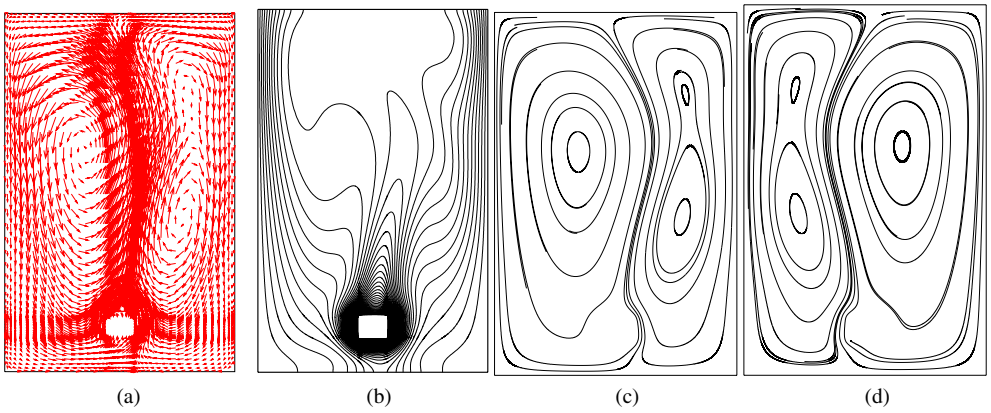

Fig. 6. Asymmetric steady state for $Ra = 1.1 \times 10^5$ in cavity $A = 2$. Velocity field (a), temperature contours (b), streamlines (c, d) for two different initial conditions.

conditions for computations at $Ra = 1.1 \times 10^5$. The asymmetric steady state which was obtained for this value of Ra can be deduced from the previous one by symmetry (Fig. 6(d)).

From a more physical point of view, we would like to emphasize two points:

- After a slight deviation towards one of the sidewalls, the upper end of the thermal plume moves back up to the center of the upper horizontal wall. When the Rayleigh number is increased, this behaviour evolves towards a configuration exhibiting a strongly deflection leading to an instability process (see Section 3.2.3).
- The streamline pattern around the heating source shows that the obstacle is fully included in the largest recirculation zone (on the left side of the figure).

Nature of the bifurcation: By gradually decreasing the Rayleigh number from $Ra = 1.1 \times 10^5$ to $Ra = 4 \times 10^4$, no hysteresis effect could be evidenced which is a first

indication that the bifurcation is probably supercritical. To confirm this point, the steady asymmetric flow was computed for a value $Ra = 5.0 \times 10^4$ slightly above Ra_c and the unstable symmetric steady base flow for this same value of Ra was also computed. The comparison between the two flows are displayed in Fig. 7, where contours of the temperature difference and plots of the velocity differences are displayed. The resulting perturbation fields clearly exhibit a symmetry opposed to the symmetry of the unstable base flow as it could be expected since the bifurcation breaks the natural symmetry of the problem. However, when Ra is slightly increased and kept within the steady range, this opposite symmetry is quickly no more visible. We believe that this is due to the competition with another instability mode similar to the mode that governs the first transition in the cavity with aspect ratio $A = 4$. However, more work would be needed to clarify this issue.

Finally, the variation of the squared amplitude of the horizontal velocity u with respect to the Rayleigh number Ra at point $M_3(0.5, 0.56)$ is plotted in Fig. 8. The linear pattern of the plot confirm the supercritical nature of the pitchfork bifurcation and allows us to compute by linear extrapolation an estimation of the critical value Ra_c of the Rayleigh number as $Ra_c = 4.8 \times 10^4$.

Comparison with the Boussinesq case: The goal of this section is to evidence the necessity of considering non-Boussinesq effects. For this purpose, calculations under the Boussinesq approximation have also been carried out in the $A = 2$ configuration. Starting from $Ra = 4 \times 10^4$ and gradually increasing the Rayleigh number, the first bifurcation point corresponding to the transition from a symmetric steady state to an asymmetric steady state appears at a critical Rayleigh number in the range $7.0 \times 10^4 < Ra_c < 7.5 \times 10^4$, therefore yielding a critical value larger than in the non-Boussinesq case. Probably more important is the onset of hysteresis effects in the vicinity of this point, revealing the subcritical nature of the transition unlike in the non-Boussinesq case. To illustrate this point, a symmetry indicator I_T for the temperature (equal to zero when the temperature field is perfectly symmetric with respect to the vertical centerline) was defined as

$$I_T = \int \int_{\Omega} (T(x,y) - T(1-x,y))^2 \, \mathrm{d}x \, \mathrm{d}y$$

The variations of this indicator for increasing Ra and for decreasing Ra are displayed in Fig. 9. Two main features are observed:

- When Ra is increased, the symmetric steady solution jumps on a branch with finite amplitude consisting in an asymmetric solution, confirming the subcritical nature of the bifurcation.
- When Ra is decreased from a point on the finite amplitude branch, the asymmetric solution persists for values of Ra down to 6×10^4, yielding multiple solutions in a finite range of Ra.

These results clearly show that even for relatively low values of ϵ, taking into account non-Boussinesq effects may be necessary.

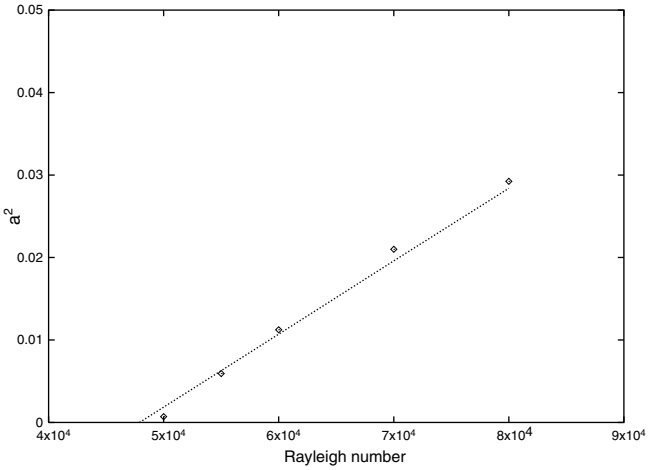

Fig. 8. Squared amplitude of the horizontal component u of velocity versus the Rayleigh number at point $M_3(0.5, 0.56)$ in asymmetric steady regime.

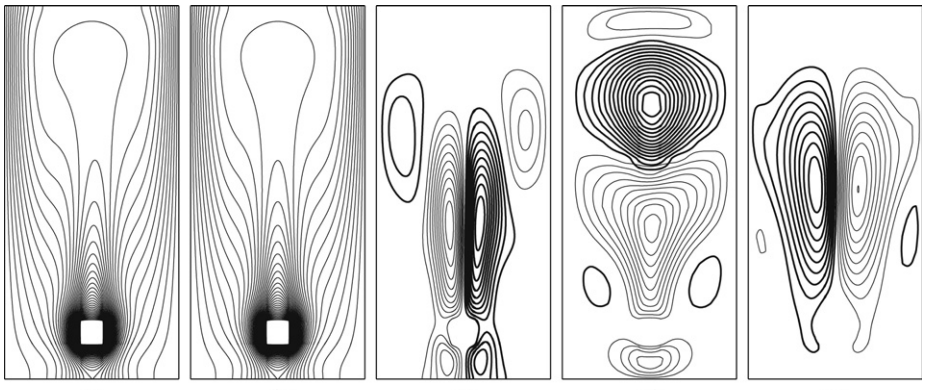

Fig. 7. (a) Temperature field at asymmetric steady state, (b) the symmetric base flow, (c) temperature disturbances, (d) u-disturbances and (e) v-disturbances for $Ra = 5.0 \times 10^4$ in cavity $A = 2$, thin (thick) lines for positive (negative) fluctuations.

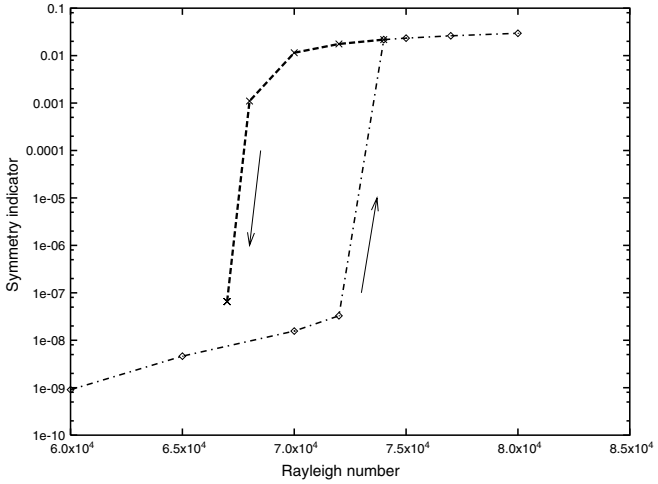

Fig. 9. Variation of the symmetry indicator I_T of the temperature field versus the Rayleigh number in the Boussinesq case.

3.2.3. Unsteady periodic flow

The asymmetric steady solutions persist for values of Ra up to 1.1×10^6. Beyond this value, the flow becomes periodic. For instance, Fig. 10(a) shows time evolution of the horizontal component u at the sampling point $M_3(0.5, 0.56)$ for $Ra = 1.3 \times 10^6$. It turns out that the signal is monochromatic. This is confirmed by its power spectrum which exhibits a fundamental frequency $f_1 = 0.145$ and its first and second harmonics, as it could be expected due to the asymmetric nature of the base flow (see Fig. 10(b)).

When decreasing the Rayleigh number from $Ra = 1.3 \times 10^6$ to $Ra = 1.1 \times 10^6$, the flow reverts to a steady and asymmetric state indicating a supercritical Hopf bifurcation.

Flow structure: For this same Rayleigh number $Ra = 1.3 \times 10^6$, typical instantaneous velocity, streamlines and temperature fields are displayed in Fig. 11(a)–(c). It should be pointed out that the thermal plume remains deflected towards one opposite vertical wall and its oscillatory motion develops around a deflected mean position. In addition, it can be noticed that the thermal plume behaves like an oblique jet impacting on a vertical wall. After the plume impacts on the right wall, the flow is distributed on each side of the impact. One part of the flow moves towards the upper wall inducing a secondary small eddy in the right top corner of the cavity while the other part moves down along the vertical wall. These two flows return then to the source, forming two primary recirculation zones, one of them including the heating source.

Temperature and vertical velocity profiles at different heights above the source are plotted in Fig. 11(d) and (e). These plots clearly exhibit the development of shear layers in the plume and near the top and vertical walls. This phenomenon is simply the continuation of the trend that was observed in the previous sections, the shear layers becoming thinner and thinner.

Mean flow and fluctuations: The time averaged flow for this same Rayleigh number was computed by integrating instantaneous solutions over a sufficiently long time. The structure of this mean flow is similar to that one of the instantaneous flow. In particular, it exhibits a thermal plume impacting on one lateral wall (see Fig. 12(a)).

The fluctuating fields were computed by subtracting the mean field from instantaneous fields. Spatial distributions of these fluctuations are displayed in Fig. 12 at four instants evenly spaced over one time period. The temperature fluctuations are essentially located within the plume, near the top wall and along the vertical right wall towards which the plume is deviated. The disturbances consist of positive and negative elongated structures distributed in the shear layers. The maximum amplitude of these fluctuations varying in the range $[-0.01, 0.01]$ are located within the plume at positions close to the source. Moreover, one can notice that the left recirculation zone of the primary flow is more stable than the right one. The fluctuations fill the full domain of the right recirculation roll, whereas they are essentially distributed at the top wall and along the plume in the largest left one.

Instability mechanisms: Examination of the instantaneous streamlines suggests that the instability arises from the impact of the thermal plume on the sidewall. Actually,

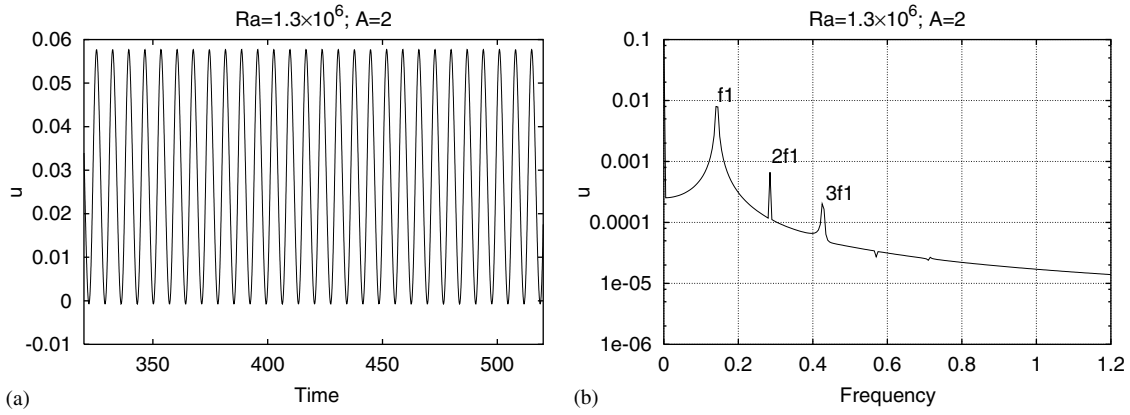

Fig. 10. (a) Time evolutions of the horizontal component u at point $M_3(0.5, 0.56)$, (b) power spectrum of u for $Ra = 1.3 \times 10^6$ in cavity $A = 2$.

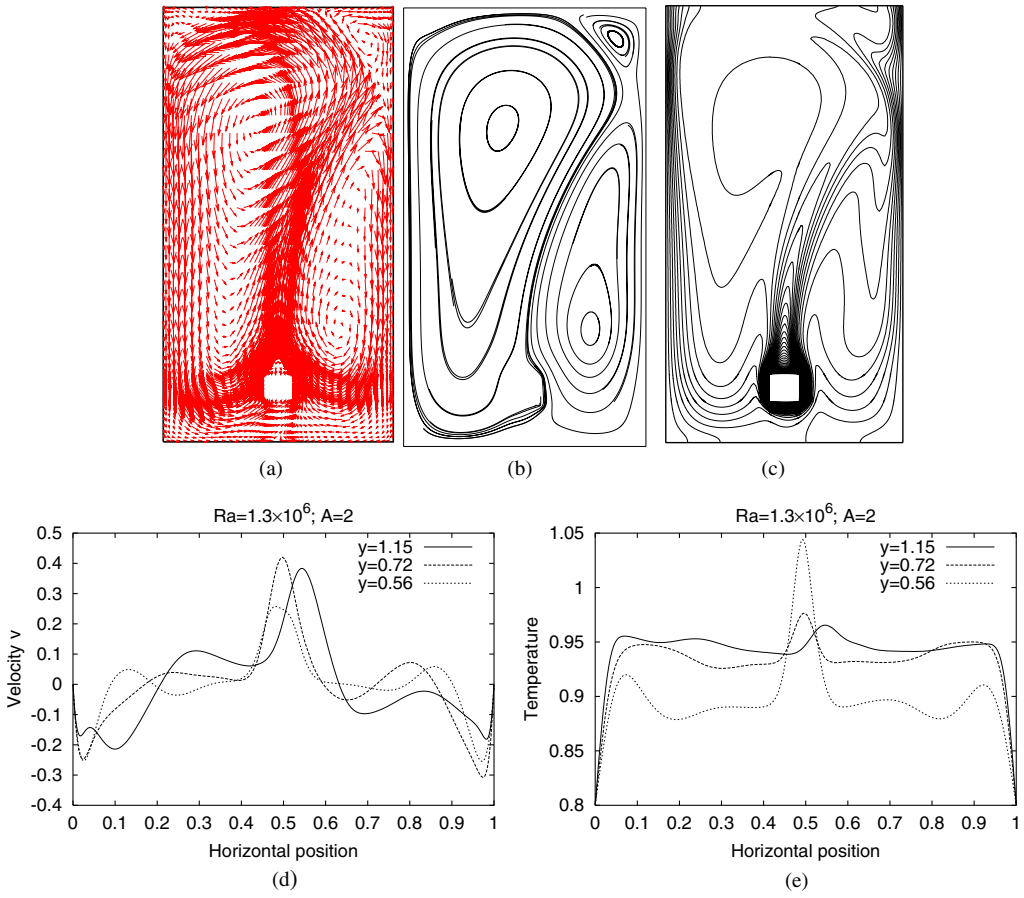

Fig. 11. (a–c) Velocity field, streamlines and isotherms at periodic state in cavity $A = 2$, (d, e) the corresponding temperature and vertical velocity profiles for $Ra = 1.3 \times 10^6$.

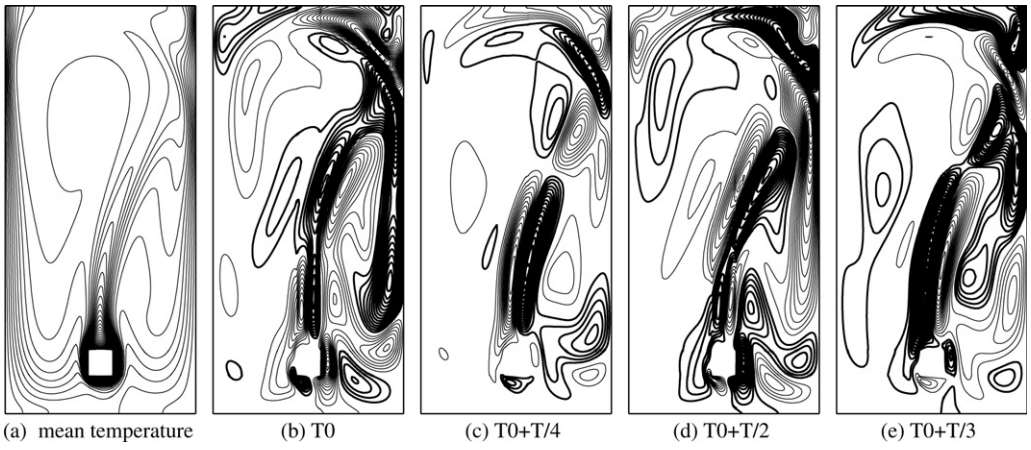

Fig. 12. (a) Mean temperature field, (b–e) temperature fluctuations for $Ra = 1.3 \times 10^6$ at four equally spaced times; thin (thick) lines for positive (negative) fluctuations, variation range $[-0.01, +0.01]$, cavity $A = 2$.

we have checked that, in steady asymmetric case, the deflection of the plume grows when the Rayleigh number increases. This phenomenon persists until the plume reaches the wall. The plume then splits in two parts as described in the previous section, leading to the instability process.

3.3. Cavity $A = 4$

3.3.1. Symmetric steady flow

An asymptotic symmetric steady flow is found for Rayleigh numbers lower than $Ra = 1.3 \times 10^4$. Typical velocity and temperature fields are displayed for $Ra = 1.2 \times 10^4$ in

Fig. 13(a) and (b). As seen in the previous cases, two symmetric recirculation flows delimited by an ascending thermal plume can be observed. However, the plume in this case, does not extend to the top wall and a separated shear layers regime is no longer observed. Horizontal profiles of temperature and vertical velocity at three vertical positions above the source for the same Rayleigh number are displayed in Fig. 13(c) and (d). These profiles are similar to those of Poiseuille-type flows except in the upper part of the cavity where the fluid is at rest.

3.3.2. Unsteady periodic motion

When increasing the Rayleigh number beyond $Ra = 1.2 \times 10^4$, the flow looses its stability. The transition occurs at a critical value Ra_c in the range $[1.2 \times 10^4, 1.3 \times 10^4]$. As it could be expected because of the larger distance between the horizontal walls, the flow becomes unstable for lower values of the Rayleigh number than in the previous cases $A = 1$ and $A = 2$. Time evolutions of the horizontal component u indicate that the flow undergoes a transition to a periodic state. The power spectrum of the horizontal velocity u indicates a very low value ($f_1 = 0.05$) of the frequency and the absence of any harmonics (see Fig. 14).

Flow structure: Typical instantaneous velocity and temperature fields are displayed for this same Rayleigh number in Fig. 15(a) and (b) and Fig. 15(f) and (g) at two instants taken over one time period. We can see that the swaying motion of the plume is of sinusoidal type as in the case of a freely rising plume. Because of the low Rayleigh number, the amplitudes of oscillations are very weak.

Mean and base flow: The time averaged temperature and velocity fields are displayed in Fig. 15(c) and (h). Noteworthy is the fact that the mean velocity field exhibits a slightly asymmetric behaviour in the middle part of the cavity whereas a possible asymmetry of the temperature field is barely visible.

To clarify this point, it was found necessary to compute the unstable symmetric steady base flow and to examine the differences between this base flow and the time averaged flow. These differences respectively are displayed in

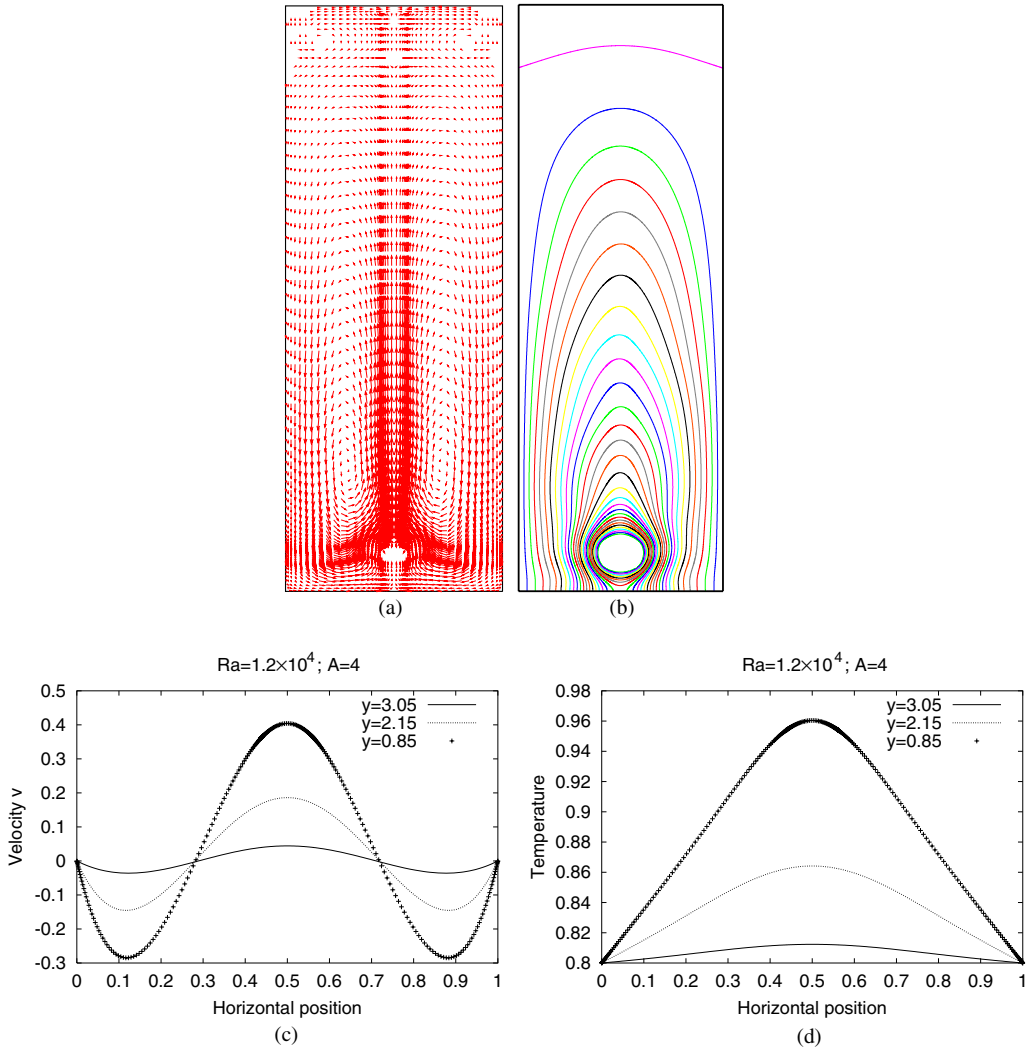

Fig. 13. (a, b) Velocity field and isotherms at steady state in cavity $A = 4$, (c, d) the corresponding temperature and vertical velocity profiles for $Ra = 1.2 \times 10^4$.

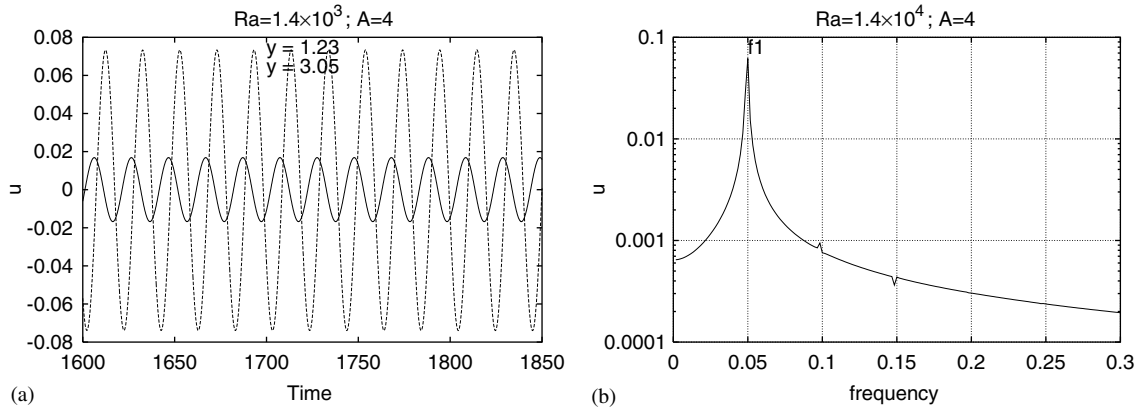

Fig. 14. (a) Time evolutions of the horizontal velocity at points $M_4(0.5, 1.23)$ and $M_5(0.5, 3.05)$, (b) power spectrum of the u-velocity at point $M(0.5, 2.15)$.

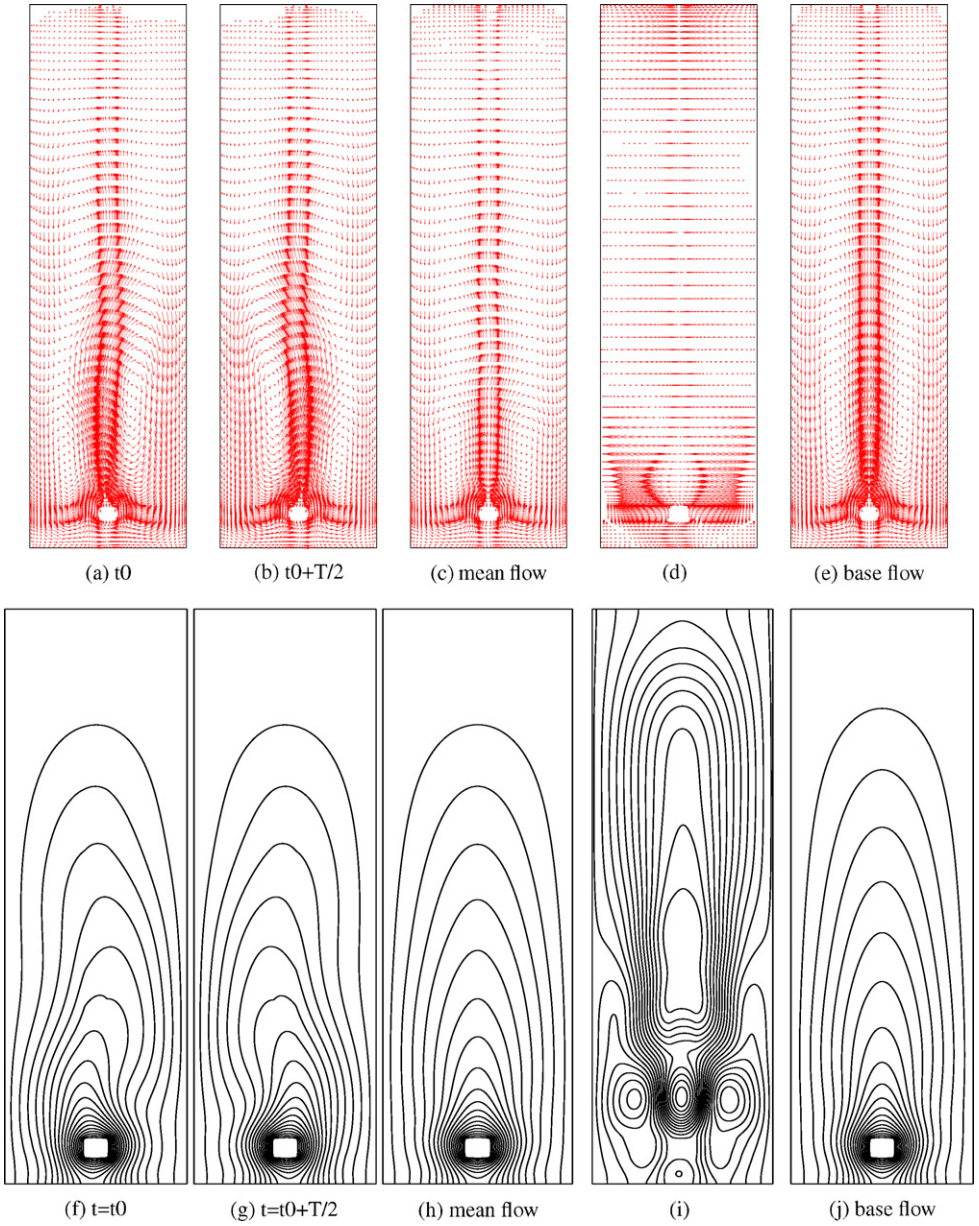

Fig. 15. (a, b) Instantaneous velocity fields at instants t_0 and $t_0 + T/2$, (c) mean velocity field, (d) difference between the mean and base flow, (e) base flow velocity, (f, g) instantaneous temperature fields, (h) mean temperature, (i) difference between the mean and base flow in the range $[-0.007, 0.004]$, (j) base flow temperature; $Ra = 1.4 \times 10^4$ and cavity $A = 4$.

Fig. 15(d) for the velocity field and in Fig. 15(i) for the temperature field. The velocity field exhibits a slight asymmetric behaviour whereas no asymmetry is visible for the temperature. In Fig. 16(a) and (b) horizontal profiles of the u component are plotted at two vertical positions above the heating source. For locations sufficiently close to the source, u-profile of the mean flow shows an asymmetric behaviour with respect to the vertical centerline by comparison with the symmetric base solution. As one moves away from the source, the difference between the base solution and the average field vanishes (Fig. 16(b)). Concerning the vertical component v of the mean flow, the horizontal profiles (not shown here) remain symmetric and very close to those of the base flow whatever the height.

Flow fluctuations: For the purpose of comparison with the previous cases $A = 1$ and $A = 2$, spatial distributions of temperature and velocity fluctuations with respect to the symmetric base solution are displayed in Fig. 17 for $Ra = 1.4 \times 10^4$ at eight instants over one time period. The figures show that the instabilities patterns are substantially

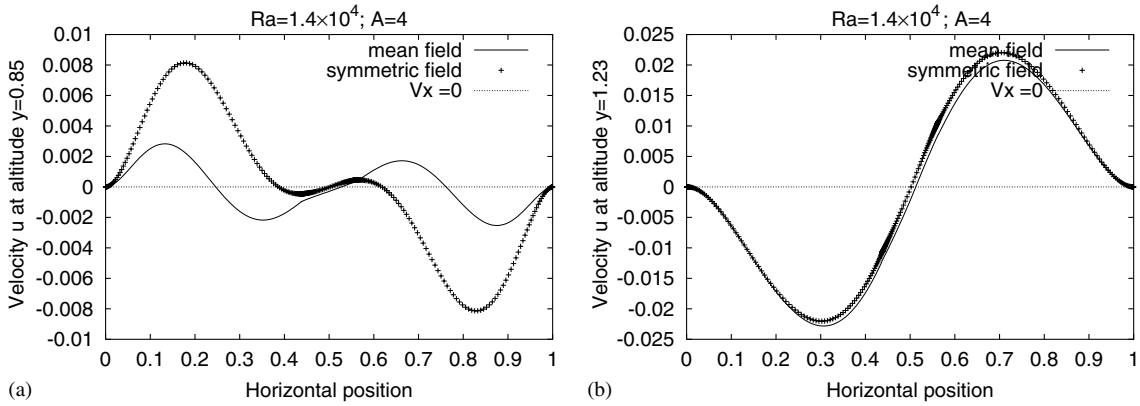

Fig. 16. Horizontal profiles of u-velocity for $Ra = 1.4 \times 10^4$: (a) at $y = 0.85$, (b) at $y = 1.23$, comparison between the mean and base flows.

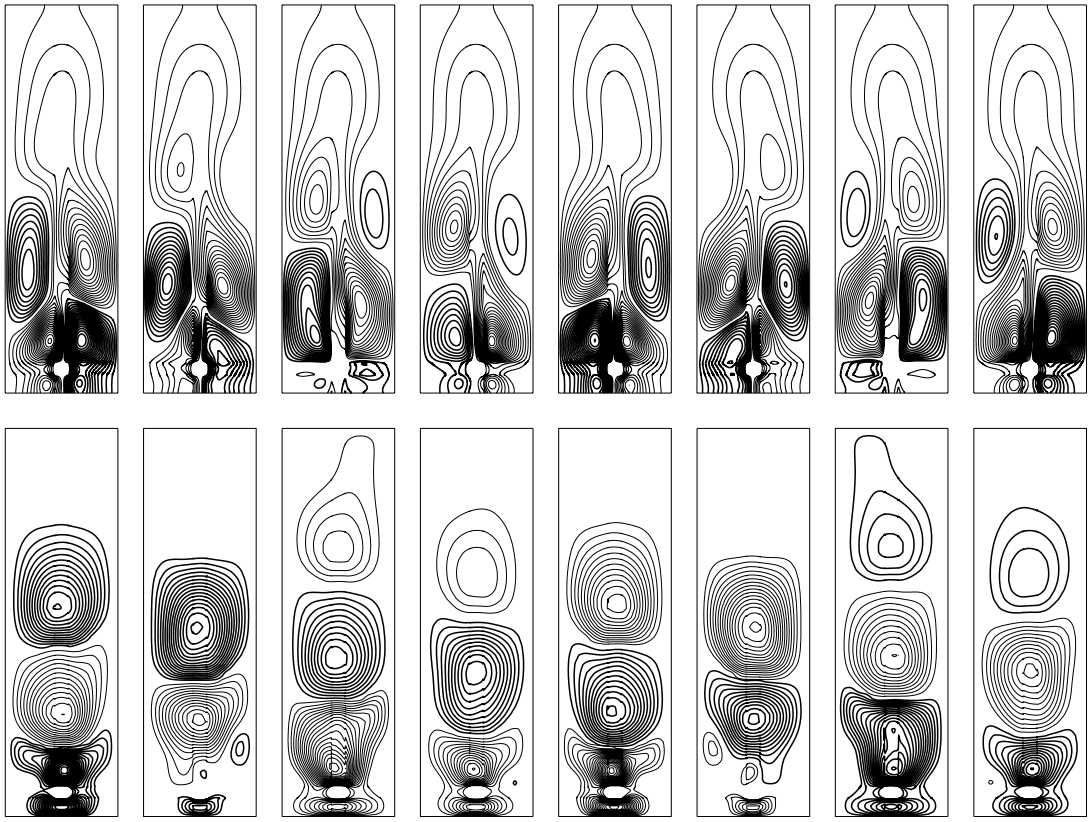

Fig. 17. Temperature fluctuations (at the top row) and u fluctuations (below) for $Ra = 1.4 \times 10^4$ at eight instants with a time step $= T/8$; thin (thick) lines for positive (negative) fluctuations. Variation range for temperature fluctuations $[-0.03, +0.025]$, variation range for u velocity fluctuations $[-0.1, +0.11]$, cavity $A = 4$.

different from those observed in the previous cases. Actually, the disturbances grow and spread out over the full flow domain. In addition, they have a preferred downward propagation direction in spite of the flow direction in the middle part of the cavity. Temperature and vertical velocity fluctuations (not shown here) are organized as large cells constituted of pairs of superimposed positive and negative perturbations occupying the whole width of the cavity. Those of the horizontal velocity are structured as single "circular" cells of positive and negative values alternately superimposed in the vertical direction. Supported by dynamical sequences, it was found that the disturbances originate from the unstable layer of fluid at the top of the cavity, then move down in the vertical direction until they reach the bottom wall. Their periodic motion is comparable with a wave whose propagation speed is uniform and directed downwards.

The physical mechanism leading to this type of instability is different from that one found in the square cavity implying shear layers with large velocity gradient. Here, the absence of sheared zones suggests that only the buoyancy forces are responsible for the disturbance development. This type of instability has been demonstrated to be due to nonlinear density variation with temperature [25], this is why large disturbances are located in the high-density region. The buoyancy forces which act downward near the cold vertical walls where the fluid is denser cause strong downward disturbances flow that explains a preferred direction of disturbances propagation: from top to bottom.

This second type of instability behaves like the so-called 'buoyancy-driven instabilities' which were already reported in previous works [26–28] for non-Boussinesq mixed convection in a tall vertical channel. The recent investigations carried out by Suslov [28] show a stability diagram for a wide range of Grashof and Reynolds numbers indicating the influence of the governing parameters (Gr, Re) on the appearance of the two distinct modes of instabilities: shear and buoyancy-driven instabilities.

4. Conclusions

In this paper, natural convection flows in a rectangular two-dimensional cavity have been numerically studied. The flows under consideration are generated by large temperature differences between a square solid obstacle kept at a constant hot temperature and walls kept at a constant cold temperature. In order to avoid too stringent stability criterion in the numerics, the acoustic waves have been filtered out by considering the compressible Navier–Stokes equations under the low Mach number approximation.

Only moderate values of the Rayleigh number have been considered. More specifically, we were interested in the first bifurcation undergone by the flow, and possibly the second, when the Rayleigh number is increased. An important point which was considered within this context, is that there exists a natural reflection symmetry with respect to the mid vertical axis for this problem, whatever the value of the aspect ratio A.

The main results may be summarized as follows:

- For sufficiently low values of the Rayleigh number, a steady symmetric flow is obtained whatever the value of the aspect ratio A. This flow consists of two large recirculation cells, one in each half of the cavity, which isolate a quiet fluid layer, uniform in temperature, below the heating source.
- For sufficiently large values of the Rayleigh number, the flow becomes unsteady in a periodic manner. However, if the transition to unsteadiness occurs directly from the previous symmetric steady flow through a supercritical Hopf bifurcation for $A = 1$ and $A = 4$, it is not the case for $A = 2$ where the flow undergoes firstly a supercritical pitchfork bifurcation leading to an asymmetric steady state deflected towards one of the sidewalls. This asymmetric state then undergoes a supercritical Hopf bifurcation leading to an oscillatory motion around a deflected mean flow.
- The instabilities which occur through the different Hopf bifurcations are not all of the same type, depending on the aspect ratio A. For $A = 1$ and $A = 2$, they are shear layer instabilities, whereas for $A = 4$ they are bulk instabilities which were referred by Suslov as buoyancy instabilities. In our case, they take the form of travelling waves which fill the whole cavity and propagate downwards with a well defined phase velocity.
- All the bifurcations that were encountered broke the natural symmetry of the problem.

In these computations, the only parameter to be varied, apart from the Rayleigh number, was the aspect ratio A. Along these lines, computations will be carried out in future considering larger values of the aspect ratio for which a wider range of instabilities may be expected. In particular, the results that were obtained by Weisman et al. [30] suggest that subcritical bifurcation could be found.

However, it is clear that the influence of other parameters have to be considered in future works. In particular, increasing the temperature difference, i.e. the parameter ϵ, would likely lead to different flow structures and instabilities.

Acknowledgement

The computational time on a NEC-SX5 computer was provided by IDRIS, the computation center of the French CNRS, under project #1102.

References

[1] T. Fujii, Theory of the steady laminar natural convection above a horizontal line heat source and a point heat source, Int. J. Heat Mass Transfer 6 (1963) 597–606.

[2] B. Gebhart, L. Pera, A.W. Schorr, Steady laminar natural convection plumes above a horizontal line heat source, Int. J. Heat Mass Transfer 13 (1970) 161–171.

[3] T. Fujii, I. Morioka, H. Uehara, Buoyant plume above horizontal line heat source, Int. J. Heat Mass Transfer 16 (1973) 755–768.
[4] L. Pera, B. Gebhart, On the stability of laminar plumes: some numerical solutions and experiments, J. Heat Mass Transfer 14 (1971) 975–984.
[5] S.E. Haaland, E.M. Sparrow, Stability of buoyant boundary layers and plumes taking into account of nonparallelism of the basic flows, Trans. ASME: J. Heat Transfer 95 (1973) 295–301.
[6] S. Wakitani, H. Yosinobu, Stability characteristics of a natural convection flow above a horizontal line heat source, J. Phys. Soc. Jpn. 53 (1984) 1291–1300.
[7] S. Wakitani, Non-parallel-flow stability of a two-dimensional buoyant plume flow, J. Fluid Mech. 159 (1985) 241–258.
[8] R.G.H. Bill, B. Gebhart, The transition of plane plume, Int. J. Heat Mass Transfer 18 (1975) 513–526.
[9] H. Yosinobu, Y. Onishi, S. Amano, S. Enyo, S. Wakitani, Experimental study on instability of a natural convection flow above a horizontal line heat source, J. Phys. Soc. Jpn. 47 (1979) 312–319.
[10] R.J. Forstrom, E.M. Sparrow, Experiments on the buoyant plume above a heated horizontal wire, Int. J. Heat Mass Transfer 10 (1967) 321–331.
[11] A.W. Schorr, B. Gebhart, An experimental of natural convection wakes above a line heat source, Int. J. Heat Mass Transfer 13 (1970) 557–571.
[12] Y. Jaluria, Thermal plume interaction with vertical surfaces, Lett. Heat Mass Transfer 9 (1982) 107–117.
[13] L. Pera, B. Gebhart, Laminar plume interactions, J. Fluid Mech. 68 (1975) 259–271.
[14] G. Desrayaud, G. Lauriat, Unsteady confined buoyant plumes, J. Fluid Mech. 252 (1993) 617–646.
[15] J.L. Zia, M.D. Xin, H.J. Zhang, Natural convection in an externally heated enclosure containing a local heat source, J. Thermophys. 4 (2) (1990) 233–238.
[16] A. Horvat, I. Kljenak, J. Marn, On incompressible flow benchmarking, Numer. Heat Transfer 39 (2001) 61–78.
[18] S. Paolucci, On the filtering of sound from the Naviers–Stokes equations, Sandia National Laboratory Report SAND 82-8257 (1982) 3–52.
[19] D.R. Chenoweth, S. Paolucci, Natural convection in an enclosed vertical air layers with large horizontal temperature differences, J. Fluid Mech. 169 (1986) 173–210.
[20] P. Le Quéré, R. Masson, P. Perrot, A Chebyshev collocation algorithm for 2D non-Boussinesq convection, J. Comput. Phys. 103 (1992) 320–335.
[21] H. Mlaoulah, T. Tsuji, Y. Nagano, A study of non-Boussinesq effect on transition of thermally induced flow in a square cavity, Int. J. Heat Fluid Flow 18 (1997) 100–106.
[22] B. Zappoli, S. Amiroudine, P. Carlès, J. Ouazzani, Thermoacoustic and buoyancy driven transport in a square side-heated cavity filled with a near-critical fluid, J. Fluid Mech. 316 (1996) 53–72.
[23] B. Zappoli, A. Jounet, S. Amiroudine, A. Mojtabi, Thermoacoustic heating and cooling in near-critical fluids in the presence of a thermal plume, J. Fluid Mech. 388 (1999) 389–409.
[24] K. Goda, A multistep technique with implicit difference schemes for calculating two or three dimensional cavity flows, J. Comput. Phys. 30 (1979) 76–95.
[25] S.A. Suslov, S. Paolucci, Stability of mixed convection flow in a tall vertical channel under non-Boussinesq conditions, J. Fluid Mech. 302 (1999) 91–115.
[26] S.A. Suslov, S. Paolucci, Nonlinear stability of mixed convection under non-Boussinesq conditions. Part 1. Analysis and bifurcations, J. Fluid Mech. 398 (1999) 61–85.
[27] S.A. Suslov, S. Paolucci, Nonlinear stability of mixed convection under non-Boussinesq conditions. Part 2. Mean flow characteristics, J. Fluid Mech. 398 (1999) 87–108.
[28] S.A. Suslov, Multi-mode spatio-temporal instability in non-Boussinesq convection, ANZIAM J. 45 (2004) 149–162.
[29] P. Le Quéré, C. Weisman, H. Paillère, J. Vierendeels, E. Dick, R. Becker, M. Braack, J. Locke, Modelling of natural convection flows with large temperature differences: a benchmark problem for low Mach number solvers. Part 1. Reference solutions, M2AN 39 (3) (2005) 609–616.
[30] C. Weisman, D. Barkley, P. Le Quéré, in: R. Bennacer, A.A. Mohamad, M. El Ganaoui, J. Sicard (Eds.), Progress in Computational Heat and Mass Transfer, Lavoisier, Paris, 2005, pp. 15–18.